ORIGINAL PAPER

Preparation and characterization of $Ca_{1-x}Ce_xMnO_3$ perovskite electrodes

C. Lucas · I. Eiroa · M. R. Nunes · P. A. Russo ·
M. M. L. Ribeiro Carrott · M. I. da Silva Pereira ·
M. E. Melo Jorge

Abstract The electrochemical properties of $Ca_{1-x}Ce_xMnO_3$ perovskite-type oxide electrode have been investigated by cyclic voltammetry in Na_2SO_4 aqueous solutions with pH 14. The structural and morphological characterizations have also been investigated and the information used to interpret the electrochemical behavior. An estimation of the electrode's capacitance and roughness factor has been obtained by means of cyclic voltammetry. The specific capacitance and consequently the roughness factor values are affected by the presence of Ce ions in the oxide. These findings are in agreement with the increase of the oxide-specific surface area by the introduction of Ce ion. The open-circuit potential and the voltammetric patterns are dependent on the presence of Ce ion in the electrodes and support that the surface electrochemistry of the perovskite oxide electrodes is governed by the Mn^{4+}–Mn^{3+} redox couple.

Keywords Perovskites · Manganites · Electrodes · Cyclic voltammetry · BET

C. Lucas · I. Eiroa
Departamento de Química e Bioquímica, Faculdade de Ciências,
Universidade de Lisboa,
Lisbon, Portugal

M. R. Nunes · M. I. da Silva Pereira (✉) · M. E. Melo Jorge
Departamento de Quimica e Bioquímica, CCMM, FCUL,
Universidade de Lisboa,
Campo Grande C8,
1749-016 Lisbon, Portugal
e-mail: mipereira@fc.ul.pt

P. A. Russo · M. M. L. Ribeiro Carrott
Departamento de Química, Centro de Química de Évora,
Universidade de Évora,
Évora, Portugal

Introduction

Perovskite-type oxides, ABO_3, with transition metals attract much attention because the substitution of aliovalent ions for A site and B site positions leads to interesting variations on their chemical and physical properties. These materials present important properties namely high electronic conductivity, mobility of the oxide ions in the crystal, and variations on the oxygen content, leading to promising candidates for electrode materials with technological applications. A variety of electrode materials with perovskite-type structure have been exploited in the past for their application in electrochemical sensors, fuel cells and as oxidation or reduction catalysts [1–8].

The electrocatalytic properties of $La_{1-x}Sr_xMnO_3$ for the reduction of oxygen have been investigated by Hammouche et al. [4]. The authors claimed that the improvement, observed on the oxide electrochemical activity, is due to an extension of the active sites for oxygen reduction, as a result of oxygen vacancy formation inside the material. Another study, carried out by Morimoto et al. [5], involved the $Ca_{1-x}La_{2x/3}MnO_{3-\delta}$ compounds. They found that these samples show high electronic conductivity and could work as active materials, in alkaline batteries, without any conductive materials. On the other hand, studies concerning the properties of $Ca_{1-x}Ce_xMnO_{3-\delta}$ oxide system, prepared by the ceramic method indicate these materials as possible candidates for cathode materials in alkaline batteries [9, 10].

We have recently explored the possibility of preparing the $Ca_{1-x}Ce_xMnO_{3-\delta}$ oxide system by the citrate route method [11]. This technique has the advantage to produce polycrystalline materials characterized by small particle size, high porosity, and uniform pore size. The electrical resistivity values for these samples show that the doping of

the $CaMnO_3$ phase with Ce ions induces, simultaneously, a marked decrease in the electrical resistivity and a metal insulator transition at high temperatures. This behavior has been attributed to the formation of Mn^{3+} ions as a result of charge compensation.

Based on the information that the $Ca_{1-x}Ce_xMnO_{3-\delta}$ oxides meet the requisites to be used as cathode materials for alkaline batteries [11], we attempt to use this new synthesis method to prepare more active electrodes without any conductive additives.

The work has been focused on the preparation and investigation of the morphological, microstructural, and electrochemical properties of $Ca_{1-x}Ce_xMnO_3$ ($x=0$, 0.1, 0.2) pelleted electrodes obtained from the powders, synthesized by the citrate route. Cyclic voltammetry was employed to study the electrochemical characteristics of the $Ca_{1-x}Ce_xMnO_3$ ($x=0$, 0.1, 0.2) electrodes, namely the effect of the replacement of Ca ions by Ce ions on the surface reactions and active surface area.

Experimental

Bulk ceramic samples were prepared from appropriate amounts of $CaCO_3$, $(NH_4)_2Ce(NO_3)_6$, and $Mn(NO_3)_2 \cdot 4H_2O$ by the citrate route method at 1,373 K as described in a previous paper [11]. However, a different heat treatment was performed. After the decomposition at 873 K, for 6 h, the resulting amorphous powder was grounded and heated in air at 1,373 K for 36 h with intermediate grinding. The oxide powder (≈200 mg) was uniformly distributed onto an inserted Pt mesh and pressed, into 1-mm-thick, ≈2-cm^2 platelet pellets under 40 bar pressure and sintered at 1,373 K, in air, for 6 h. The electrical contact was made by welding the Pt mesh to a copper wire. The samples were then mounted in a glass tube with Araldite epoxy resin, so that the electrolyte could only make contact with the oxide. Three specimens were prepared for each composition, two for the electrochemical experiments and one for morphological characterization.

The structural characterization of the polycrystalline powder and the electrodes was carried out by X-ray powder diffraction using a Philips PW 1730 X-ray powder diffractometer, operating with a monochromatized Cu-K$_\alpha$ radiation in Bragg-Brentano geometry. Lattice parameters were refined by a least-square method. The average crystallite sizes were determined by Debye–Scherrer's formula. Morphological observations of the samples were performed by scanning electron microscopy (SEM) using a JEOL (JSM-35C).

The samples' oxygen stoichiometry was determined by iodometric titration. Each sample was dissolved in potassium iodide solution and hydrochloric acid and then titrated with a standard sodium thiosulfate solution. The oxygen content was determined to be 3.00 ± 0.01. This value, led us to conclude that all the samples can be considered stoichiometric within the experimental error.

Nitrogen adsorption–desorption isotherms at 77 K were determined on a CE Instruments Sorptomatic 1990, using helium (for dead space calibration) and nitrogen of 99.999% purity supplied, respectively, by Linde and Air Liquide. Prior to the determination of the adsorption isotherms, the samples were outgassed for 8 h at 423 K, achieved using a heating rate of 2 K min^{-1}. A sample cell with dead space volume minimized by a glass rod and about 4 g of the powders were used due to the low surface area of the materials. The specific surface areas were estimated from the analysis of the adsorption isotherms by the Brunauer-Emmett-Teller (BET) method and using 0.162 nm^2 for the nitrogen cross-sectional area [12, 13].

The oxides electrochemical behavior was studied by means of open-circuit potential measurements and cyclic voltammetry, in 10^{-2} mol dm^{-3} Na_2SO_4 (pH 14) solutions. The pH was adjusted by the addition of KOH concentrated solution. Solutions were prepared from AnalaR reagents with Millipore Milli-Q water and degassed with nitrogen, 99.999% purity gas supplied by Air Liquide. The electrochemical experiments were performed in a three-compartment glass cell at room temperature. The counter electrode was a graphite rod and, as reference, an Hg/HgO (0.099 V vs. SHE) was used. Electrochemical measurements were carried out using a low-noise operational amplifier potentiostat incorporated with positive feedback IR compensation, programmed by a Bank VSG 83 waveform generator and a Kipp and Zonen Pró-1 recorder.

Results and discussion

X-ray diffraction

The X-ray diffraction (XRD) patterns show that for all compositions the samples are single phase and indexed as an orthorhombic perovskite structure in the *Pnma* space group. Figure 1 shows a representative X-ray diffraction pattern for two members of the series with $x=0$ and $x=0.2$. The splitting and the broadness of the XRD peaks, visible for $x=0.2$, indicates the increase of the structure distortion with Ce content, i.e., the orthorhombicity increases strongly with the cerium substitution. These results clearly show that $Ca_{1-x}Ce_xMnO_3$ ($0 \le x \le 0.2$) single-phase samples can be synthesized, at lower temperature, via citrate route. Previous studies, on the same system [9, 10, 14, 15], refer that only by raising the firing temperature to 1,573 K and using solid-state reactions could the phases be obtained. Our data are in excellent agreement with the results reported by Zeng
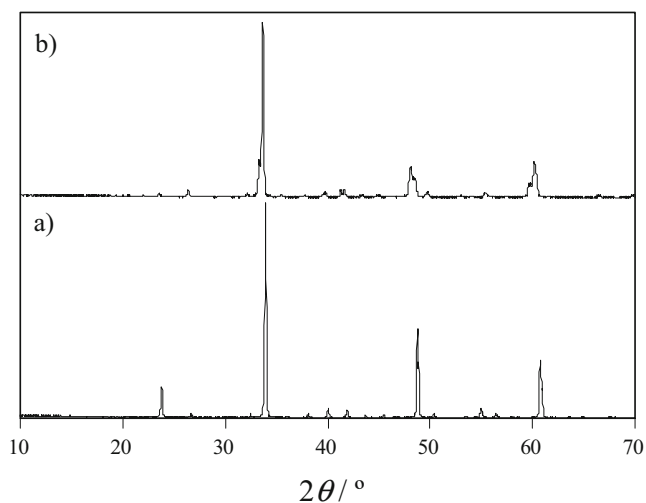
Fig. 1 X-ray diffraction patterns for **a** CaMnO$_3$ and **b** Ca$_{0.8}$Ce$_{0.2}$MnO$_3$

et al. [16] concerning the structural, magnetic, and transport properties of the Ca$_{1-x}$Ce$_x$MnO$_3$ ($x \leq 0.2$) system, synthesized by the sol-gel method also at 1,373 K.

Furthermore, from Fig. 1 it can be observed that, as the cerium content increases in the Ca$_{1-x}$Ce$_x$MnO$_3$, the diffraction peaks shift slightly to lower 2θ values, indicating that the lattice parameters increase with the increase of cerium doping level. This shift also confirms the accommodation of the cerium ion into the lattice structure.
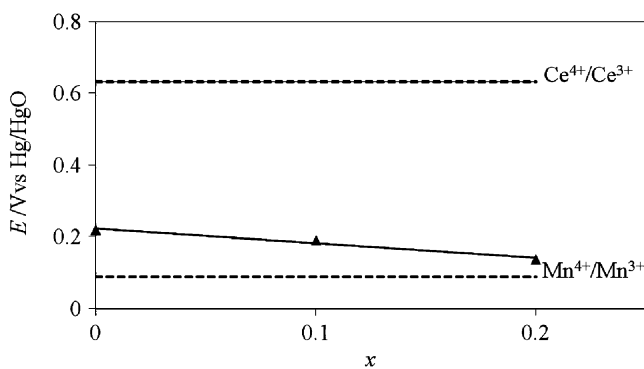
The evaluated lattice parameters are given in Table 1. The values are in good agreement with the published data [11, 16, 17]. As expected, an increase on the cell parameters, for the Ce compounds, was observed as a consequence of the successful substitution of Ca ion for Ce ion. This effect is easily understood considering that the replacement of Ca^{2+} by Ce^{4+} leads to an increase on the Mn^{3+} concentration (0.645 Å) in the structure, which is larger than Mn^{4+} (0.530 Å) [18]. Moreover, taking into account the phase ionic composition, although the effective ionic radius of Ce^{4+} (1.14 Å) is smaller than that of Ca^{2+} (1.34 Å), we can conclude that the increase on the B site (8.7%) mean ionic radius is higher than the decrease on the A site (3.0%) mean ionic radius. So an expansion of the cell volume should occur.

The powders' crystallite size were calculated from the broadening of the X-ray diffraction peaks using Scherrer's formula [19] $S = k\lambda/\beta\cos\theta$, where k is a constant, λ the

wavelength of the Cu-K$_\alpha$ radiation (1.5406 Å) and β the difference in profile widths of broadened and standard samples (in our case, a silicon standard was used): $\beta = \beta_{sample} - \beta_{standard}$ (β is the full width at half maxima (FWHM) of the XRD peaks). The data show that the crystallite size of the doped calcium manganites decreases from about 100 nm (for $x=0$), reaching the values of 69 and 71 nm for the samples with $x=0.1$ and $x=0.20$, respectively.

Open-circuit potential

Figure 2 shows the open-circuit potential values (E_{oc}) for freshly prepared Ca$_{1-x}$Ce$_x$MnO$_3$ electrodes in 1 mol dm^{-3} Na$_2$SO$_4$ at pH 14. It can be seen that, when the amount of Ce^{4+}(x) increases in the samples, the open-circuit potential value decreases. It is well known that the E_{oc} values are determined by surface redox equilibria [20]. In this work, the assignment of the obtained experimental values to a specific surface reaction is hard because there are no available thermodynamic data for the perovskite oxide system Ca$_{1-x}$Ce$_x$MnO$_3$. In order to overcome this lack of information, standard potentials for different equilibria involving Mn and Ce species, in different possible oxidation states, were evaluated for pH 14 and are presented in Table 2 [21, 22]. By comparing the experimental results with the calculated ones, it is clear that they approach the thermodynamic value expected for the Mn^{4+}–Mn^{3+} equilibrium potential. The decrease on the open-circuit potential with the increase on the amount of Ce^{4+} on the samples can be explained considering that, when the Ce^{4+} replaces the Ca^{2+} on the oxide, the amounts of Mn^{4+} and Mn^{3+} decreases and increases, respectively, in the samples [11]. As a consequence, the ratio of Mn^{4+} to Mn^{3+} gets smaller and a potential decrease is expected according to the Nernst equation. This result indicates that the Mn^{4+}–Mn^{3+} redox couple is the determinant on the surface

Table 1 Cell parameter values at 300 K for Ca$_{1-x}$Ce$_x$MnO$_3$ phases

Sample	a/Å	b/Å	c/Å	V/Å^3
CaMnO$_3$	5.284 (3)	7.46 (4)	5.270 (3)	207.8 (4)
Ca$_{0.9}$Ce$_{0.1}$MnO$_3$	5.322 (1)	7.48 (1)	5.289 (1)	210.8 (1)
Ca$_{0.8}$Ce$_{0.2}$MnO$_3$	5.378 (7)	7.49 (1)	5.317 (8)	214.3 (9)

Fig. 2 Average values of the open-circuit potential as a function of the amount of Ce (x) for the Ca$_{1-x}$Ce$_x$MnO$_3$ electrodes in 10^{-2} mol dm^{-3} Na$_2$SO$_4$ at pH 14. The equilibrium potential calculated for the redox couples Mn^{4+}–Mn^{3+} and Ce^{4+}–Ce^{3+} at pH 14 are also included (*dashed line*)

Table 2 Nernst potential values calculated for different redox pairs involving Mn and Ce species, at pH 14

	Redox pair	E/V vs Hg/HgO
1	$Mn^{2.67+}$–Mn^{2+}	−0.686
2	Mn^{3+}–$Mn^{2.67+}$	−0.237
3	Mn^{4+}–Mn^{3+}	0.089
4	Mn^{7+}–Mn^{4+}	0.491
5	Mn^{6+}–Mn^{4+}	0.504
6	Ce^{4+}–Ce^{3+}	0.633

equilibrium reaction and the potential is mainly governed by the ratio of Mn^{4+} to Mn^{3+}. These findings are consistent with the charge density values for the ions in the A and B sites of the perovskite structure presented in Table 3. A systematic change is observed in the charge density values when Ce ion is introduced in the oxide. An increase of 31% and a decrease of 30% are observed for the A site and the B site ions, respectively, with the increase on the Ce ion content. However, there is a large difference between the average values of the charge densities, 37 and 868 C mm^{-3}, respectively for A and B sites, indicating that the interactions with the water molecules will be easier with the cation on the B site. This conclusion is in accordance with those referred in the literature, concerning perovskite electrodes [23].

Surface morphology

In order to get information on the effect caused by the partial replacement of Ca by Ce on the electrodes roughness factor, cyclic voltammograms at various sweep rates were recorded, in 10^{-2} mol dm^{-3} Na$_2$SO$_4$ (pH 14) solutions, between 0.15 and 0.25 V vs. Hg/HgO, where redox transitions are minimized. Fig. 3a shows a representative family of voltammograms for a Ca$_{0.9}$Ce$_{0.1}$MnO$_3$ electrode, obtained at different sweep rates. As it can be seen, the current potential curves are almost rectangular and symmetric, characterized by an abrupt current switching when the sweep is reversed. The distortion at the switching potential is dependent upon the sweep rate and is due to solution and electrode resistances. Linear plots of the capacitive current density (i), measured at 0.2 V vs. Hg/HgO, against the sweep rate (dV/dt) were obtained and

from the slope the values of the electrodes specific capacitance (C) were estimated (Fig. 3b) according to Eq. 1.

$$C = \frac{dQ}{dV} = \frac{i}{(dV/dt)} \tag{1}$$

where Q is the charge on the electrode. The positive intercept on the density current axis is due to marginal ohmic effects.

The average values calculated for the Ca$_{1-x}$Ce$_x$MnO$_3$ electrodes' specific capacitance are presented in Table 4. The obtained values for the samples with $x=0$ are similar to those reported for the specific capacitance of MnO$_x$ nH$_2$O anodic deposits in 0.1 mol dm^{-3} Na$_2$SO$_4$ and 0.3 mol dm^{-3} KCl, respectively, ranging from 36–43 to 32–36 mF cm^{-2} [24]. For the calcium-containing oxides, the results show that the replacement of Ca ions by Ce ions causes an increase in the oxide-specific capacitance, what can be related with the increasing on the samples surface area.

Assuming a value of 60 μF cm^{-2} for the capacitance of the interface oxide–aqueous solution, the electrodes' roughness factor was calculated [25] and presented in Table 4. The data indicate that the presence of Ce ions on the oxide composition leads to electrodes with a higher surface roughness. This is consistent with the observed porous oxide morphology that suggests an easier access of the electrolyte solution into the oxide layer as can be inferred from Fig. 4, where the SEM micrographs for the Ca$_{1-x}$Ce$_x$MnO$_3$ ($x=0$ and 0.2) polycrystalline samples are shown. The micrographs clearly show that the introduction of Ce ion on the oxide samples led to smaller grains. The reduction in grain size with cerium doping leads to an increase in surface area that is in accordance with the voltammetric data.

The BET-specific surface area values, obtained by analysis of the nitrogen adsorption isotherms at 77 K, were 0.6 m^2 g^{-1} for the undoped sample and 1.4 and 1.5 m^2 g^{-1}, respectively, for samples with x of 0.1 and 0.2. These results confirm that an increase of specific area occurs by the introduction of Ce ion and correlate well with the voltammetric data with regard to the comparison between the undoped sample and the Ce-ion-doped samples. Furthermore, estimates of the roughness factor, by considering the pellets preparation conditions described in the experimental section, provide indication that the real surface areas of the electrodes are not significantly different from those obtained on the loose powders analyzed. In fact,

Table 3 Ionic composition, mean ionic radius, valence state charge density (C) values of the A and B sites for Ca$_{1-x}$Ce$_x$MnO$_3$

x	(Ca, Ce) Mn$_{1-y}^{4+}$Mn$_y^{3+}$O$_3$	$\langle r_A \rangle$/Å (A site—XII)	$\langle r_B \rangle$/Å (B site—VI)	A^{m+}	Mn^{z+}	C_A/C (mm^{-3})	C_B/C (mm^{-3})
0	CaMn^{4+}O$_3$	1.34	0.530	2	4	32	1,026
0.10	Ca$_{0.90}$Ce$_{0.10}$Mn$_{0.80}^{4+}$Mn$_{0.20}^{3+}$O$_3$	1.32	0.553	2.2	3.8	36	858
0.20	Ca$_{0.90}$Ce$_{0.10}$Mn$_{0.60}^{4+}$Mn$_{0.40}^{3+}$O$_3$	1.30	0.576	2.4	3.6	42	719

a)

0.3×10^{-3} A cm^{-2}

0.15 E/V vs Hg/HgO   0.25

b)
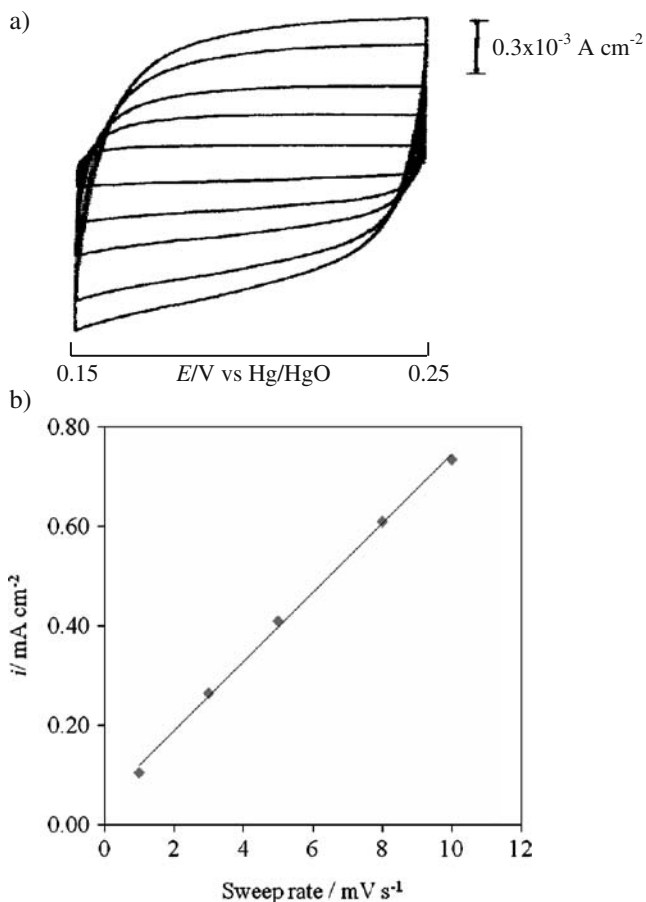
Fig. 3 **a** Cyclic voltammograms obtained in the double-layer region and **b** double-layer charging current as a function of sweep rate for a Ca$_{0.9}$Ce$_{0.1}$MnO$_3$ electrode at 0.2 V vs Hg/HgO, in 10^{-2} mol dm^{-3} Na$_2$SO$_4$ at pH 14. Sweep rates 1, 3, 5, 8, and 10 mV s^{-1}

the roughness factor values calculated from the ratio of surface area (of 200 mg of sample) to the geometrical area of the electrode (2 cm^2) [26] are 600, 1,400, and 1,500, respectively, for samples with $x=0$, 0.1, and 0.2. These values are not only of the same order of magnitude of those calculated from voltammetric data reported in Table 4 but in quite reasonable agreement, thereby suggesting that all or most of the surface area of the loose powders is accessible to the electrolyte species in the electrode pellets and that alterations may not have occurred to a great extent, upon compression and subsequent thermal treatment during the pellets preparation.

Table 4 Capacitance and roughness factor average values for Ca$_{1-x}$Ce$_x$MnO$_3$ electrodes in 10^{-2} mol dm^{-3} Na$_2$SO$_4$ solutions, pH 14, at 0.2 V vs. Hg/HgO

| x	C/10^{-3} (F cm^{-2})	Rf
0	35±11	583±11
0.1	78±5	1,300±84
0.2	98±5	1,633±81
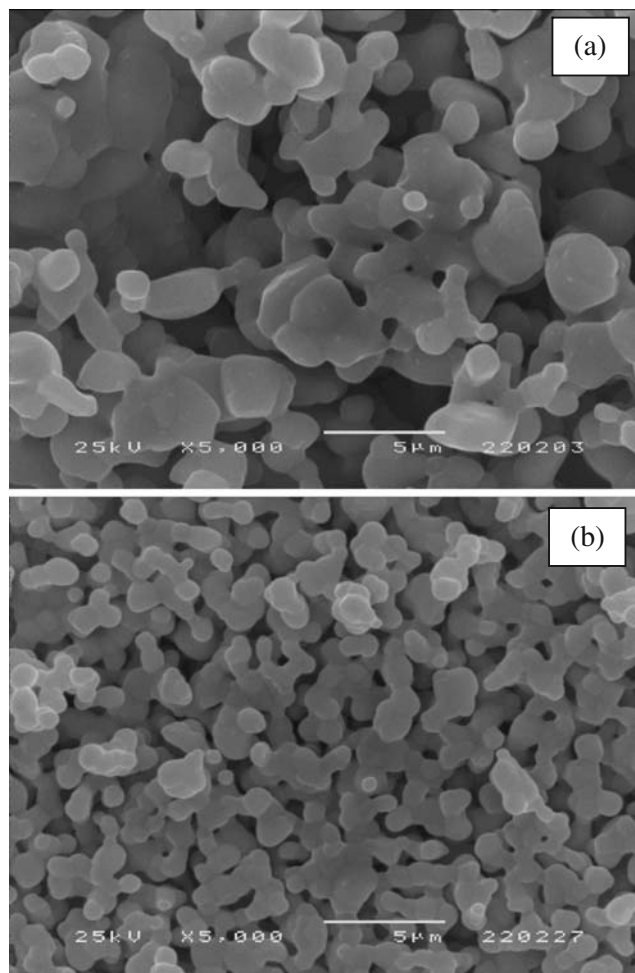
Fig. 4 SEM of Ca$_{1-x}$Ce$_x$MnO$_3$ system: **a** $x=0$ and **b** $x=0.2$

Cyclic voltammetry

Cyclic voltammograms for the Ca$_{1-x}$Ce$_x$MnO$_3$ ($x=0$, 0.1, 0.2) electrodes recorded in 1 mol dm^{-3} Na$_2$SO$_4$, pH 14, between ≈0.0 V vs. Hg/HgO and a positive limit before oxygen evolution occurs, are compared directly in Fig. 5. It can be seen that the peaks are broad, indicating a large heterogeneity in the surface sites and superposition of the redox processes concerning the metal oxide transitions [27, 28].

For all the electrodes, an anodic peak (*A1*) at approximately 0.36 V is observed, followed by an increase of current (*A*), more visible for the electrodes containing Ce ion. At this potential value, it starts to develop a violet–green color diffusing out of the electrode that increases with the increase on the potential. In what concerns the cathodic profile, three peaks (*C*, *C1*, and *C2*) are observed, peak *C* appearing as a hump for the samples with $x=0$. These experiments also show that the development of peak *C* is associated with the rising current (*A*), at potentials higher than 0.55 V. By comparing the experimentally observed potential with those presented on Table 2, it can be deduced
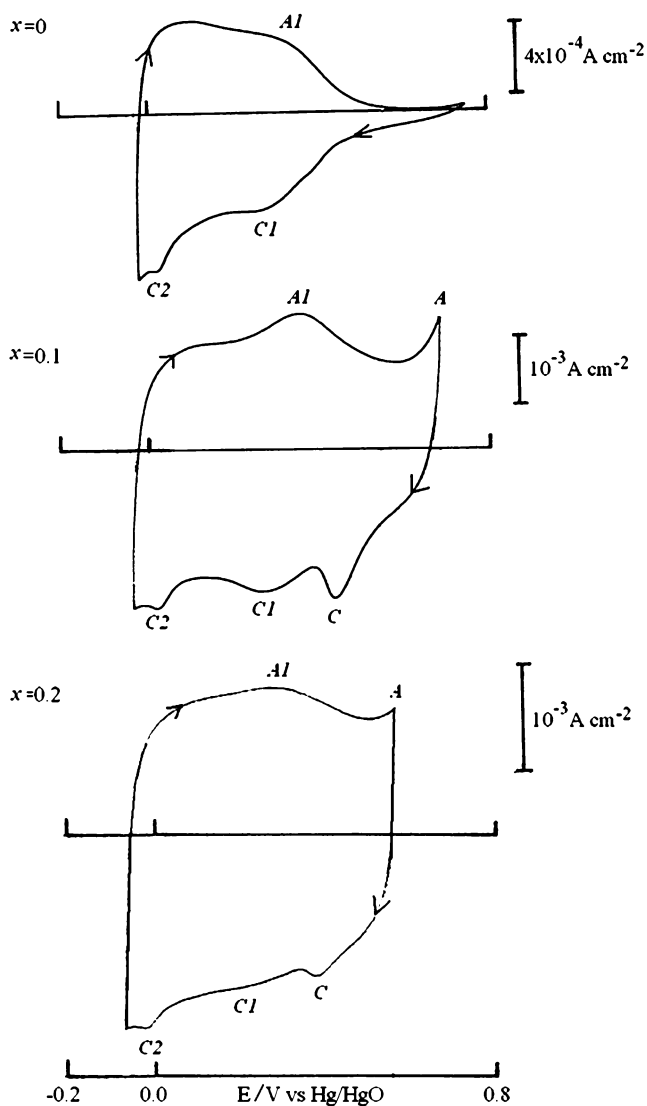
Fig. 5 Voltammetric behavior of $Ca_{1-x}Ce_xMnO_3$ ($x=0$, 0.1, 0.2) electrodes in 10^{-2} mol dm^{-3} Na$_2$SO$_4$, pH 14. Sweep rate 10 mV s^{-1}

that *A1* and the rising current (*A*) are related to the oxidation of Mn^{4+} to soluble MnO$_4^-$ and MnO$_4^{2-}$ ions (redox pairs 4 and 5). This assumption is confirmed by the visual observation of the solution coloring near the electrode in this potential region and by atomic absorption spectroscopy analysis of the solution. However, the possible overlap with oxygen evolution cannot be discarded. Indeed, the calculated value for the oxygen evolution equilibrium potential, in the used experimental conditions, is +0.302 V vs Hg/HgO.

Though the redox peaks are broad, their position can be regarded as nearly the same for all the samples. The peaks are more obvious when calcium ions are replaced with cerium ions and well defined peaks are obtained only for $x=0.1$. On the other hand, the onset of the increase of current shifts for lowers potential with the increase on the

amount of Ce ion in the oxide, presumably the presence of this ion catalyzes the oxidation process.

In order to study the influence of the positive and negative potential limits on the perovskite voltammetric behavior, voltammograms were recorded between −0.30 V and different positive limits, as well as, between 0.55 V and different negative limits. Figure 6a,b shows the data for the Ca$_{0.9}$Ce$_{0.1}$MnO$_3$ electrode in 1 mol dm^{-3} Na$_2$SO$_4$ pH 14 that illustrates the behavior of all tested electrodes.

When the negative limit is extended to −0.30 V, an additional anodic peak (*A2*) appears with a higher intensity. Moreover, the curves show clearly that the species oxidized on the anodic peak *A1* are reduced on the cathodic peak *C1*, while those oxidized on the anodic peak *A2* are reduced on the cathodic peak *C2*.

From the voltammograms, the formal potential for the redox couples associated with the peaks *A1–C1* and *A2–C2* were estimated and the obtained values are: 0.313±0.010 V and 0.053±0.010 V, respectively. By comparing these values with the calculated ones summarized on Table 2, it can be concluded that peaks *A2–C2* are associated to the Mn^{4+}–Mn^{3+} redox couple (redox pairs 3). This assignment is consistent with the fact that the oxidation states of Mn present on the perovskite electrode are Mn^{4+} and Mn^{3+}. On the other hand, *A1–C1* can be assigned to reactions involving soluble species, namely MnO$_4^-$ and MnO$_4^{2-}$ ions (redox pairs 4 and 5).
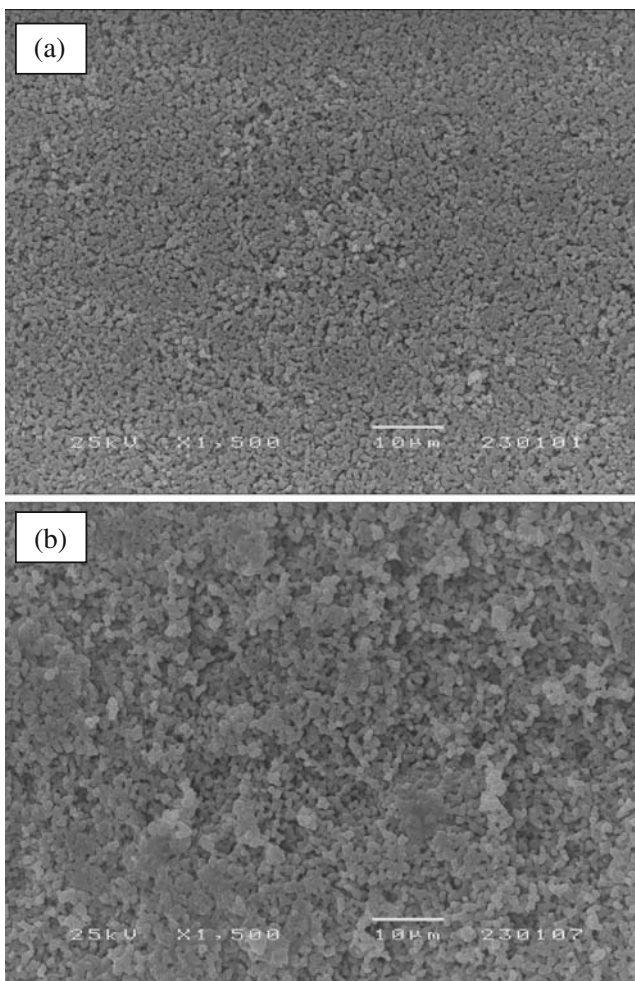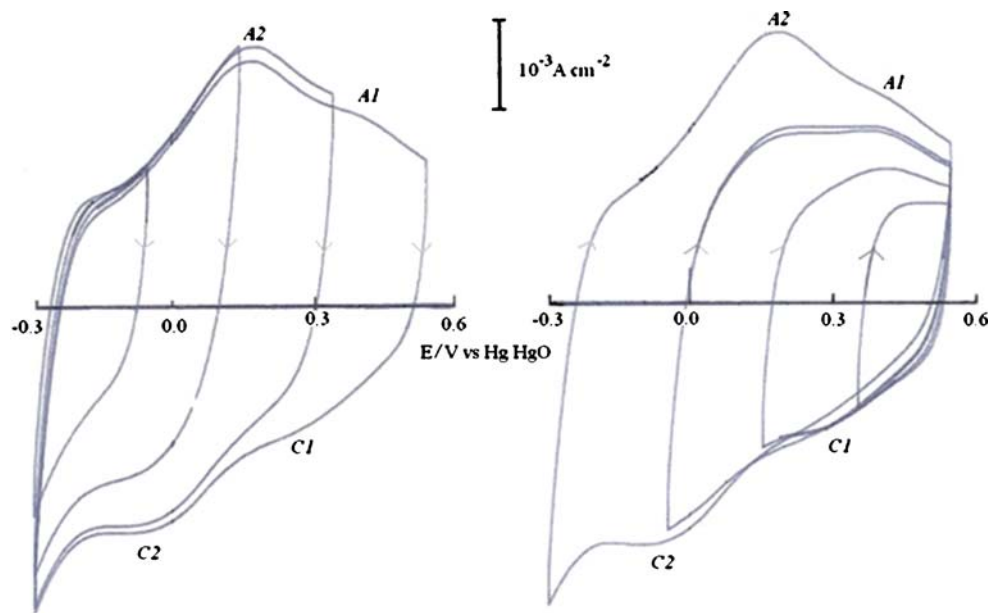
Stability

SEM coupled with the roughness factor values reveal that, after the electrochemical studies, the electrodes show a rougher and open surface, suggesting that a dissolution process has occurred at higher positive potentials. Figure 7 shows a representative micrography for a used Ca$_{0.9}$Ce$_{0.1}$MnO$_3$ electrode. These results are in accordance with the color changing of the solution when high positive potentials were applied, which is associated with the formation of manganese species with an oxidation state greater than +4. However, the perovskite structure remains after the electrochemical studies, as X-ray diffraction patterns (Fig. 8) indicates, although a slight decrease in the peaks intensity occurs.

On the contrary, the oxides are stable in the potential range between the open-circuit potential and lower negative potentials that makes possible its use as cathodes. So we are now investigating the cathodic discharge performance of these oxides in alkaline solutions.

Conclusions

Ca$_{1-x}$Ce$_x$MnO$_3$ ($x=0$, 0.1, 0.2) electrodes with high surface area were successfully prepared from the oxide powders
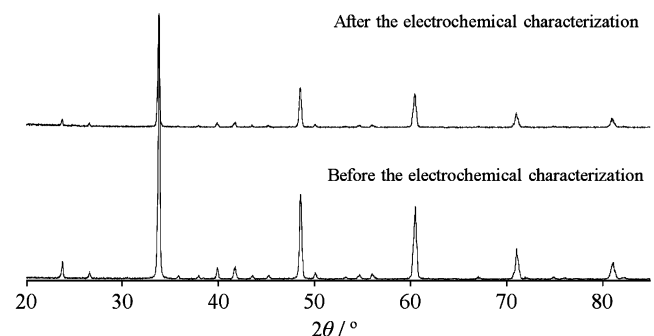
Fig. 6 Influence of the positive and negative potential limits on the voltammetric behavior of a $Ca_{0.9}Ce_{0.1}MnO_3$ electrode in 10^{-2} mol dm^{-3} Na_2SO_4 at pH 14. Sweep rate 10 mV s^{-1}

obtained by the citrate route method. The open-circuit potential values and the voltammetric patterns are dependent on the presence of Ce ion, in the electrodes, and support the assumption that the surface electrochemistry of the perovskite oxide electrodes is governed by the Mn^{4+}–Mn^{3+} redox couple.

The data also show that the amount of Ce ion affects the electrodes' specific capacitance and roughness factor values. These findings are in agreement with the data obtained for the oxide-powder-specific surface area. The increase on the capacitance values for the Ce-ion-containing electrodes has been associated with the reduction in grain size exhibited by the doped samples. These primary results indicate that the prepared $Ca_{1-x}Ce_xMnO_3$ ($x=0$, 0.1, 0.2) electrodes are promising cathode materials for alkaline batteries.

Fig. 7 SEM of the $Ca_{0.9}Ce_{0.1}MnO_3$ electrodes **a** before and **b** after electrochemical studies in 10^{-2} mol dm^{-3} Na_2SO_4, pH 14

Fig. 8 X-ray diffraction of the $Ca_{0.9}Ce_{0.1}MnO_3$ electrode before and after the electrochemical characterization in 10^{-2} mol dm^{-3} Na_2SO_4, pH 14

References

1. Bockris JO'M, Otagawa T (1984) J Electrochem Soc 131:290 doi:10.1149/1.2115565
2. Skinner SJ (2001) Int J Inorg Mater 3:113 doi:10.1016/S1466-6049(01)00004-6
3. Pereira MI, Melo MJBV, Costa FMA, Nunes MR, Peter LM (1989) J Chem Soc, Perkin Trans 1 85:2473
4. Hammouche A, Siebert E, Hammou A, Kleitz M (1991) J Electrochem Soc 138:1212 doi:10.1149/1.2085761
5. Morimoto H, Esaka T, Takai S (1997) Mater Res Bull 32:1359 doi:10.1016/S0025-5408(97)00113-X
6. Ciríaco MLF, da Silva Pereira MI, Nunes MR, Mendonça MH, Costa FM (2001) J Solid State Electrochem 5:495 doi:10.1007/s100080100227
7. Xiqiang H, Li P, Zhiguo L, Zhe L, Yu S, Zhengnan Q et al (2002) J Alloy Comp 345:265
8. Ciríaco MLF, da Silva Pereira MI, Nunes MR, Mendonça MH, Costa FM (2006) Mater Chem Phys 96:211 doi:10.1016/j.matchemphys.2005.07.005
9. Esaka T, Morimoto H, Iwahara H (1992) J Appl Electrochem 22:821 doi:10.1007/BF01023724
10. Iwahara H, Esaka T, Hamajina H (1989) Denki Kagaku 57:591
11. Melo Jorge ME, Nunes MR, Silva MR, Sousa D (2005) Chem Mater 17:2069 doi:10.1021/cm040188b
12. Singh KSW, Everett DH, Haul RAW, Moscou L, Pierotti RA, Rouquérol J et al (1985) Pure Appl Chem 57:603 doi:10.1351/pac198557040603
13. Rouquérol F, Rouquérol J, Sing KSW (1999) Adsorption by powders and porous solids. Academic, London
14. Ohtaki M, Koga H, Tokunaga T, Eguchi K, Arai H (1995) J Solid State Chem 120:105 doi:10.1006/jssc.1995.1384
15. Vecherskii SI, Konopel'ko MA, Esina NO, Batalov NN (2002) Inorg Mater 38:1270 doi:10.1023/A:1021379606219
16. Zeng Z, Greenblatt M, Croft M (2001) Phys Rev B 63:224410–224411 doi:10.1103/PhysRevB.63.224410
17. Melo Jorge ME, Correia dos Santos A, Nunes MR (2001) Int J Inorg Mater 3:915 doi:10.1016/S1466-6049(01)00088-5
18. Shannon RD (1976) Acta Crystallogr A 32:751 doi:10.1107/S0567739476001551
19. Klug H, Alexander L (1962) X-ray diffraction procedures. Wiley, New York
20. Trasatti S (1994) In: Lipkowski J, Ross PN (eds) Electrochemistry of novel materials. VCH, New York
21. Pourbaix M (1974) Atlas of electrochemical equilibria in aqueous solutions. NACE, Houston
22. Hayes SA, Yu P, O'Keefe TJ, O'Keefe MJ, Stoffer JO (2002) J Electrochem Soc 149:C623 doi:10.1149/1.1516775
23. Bockris JO'M, Khan SUM (1993) Surface electrochemistry, a molecular level approach. Plenum, New York
24. Chang C, Tsou T (2002) Electrochim Acta 47:3523 doi:10.1016/S0013-4686(02)00321-3
25. Levine S, Smith AL (1971) Discuss Faraday Soc 52:290 doi:10.1039/df9715200290
26. Wattiaux A, Grenier JC, Pouchard M, Hagenmuller P (1987) J Electrochem Soc 134:1714 doi:10.1149/1.2100741
27. Trasatti S, Kurzweil P (1994) Platinum Metal Rev 38:46
28. Mattos-Costa FI, Lima-Neto P, Machado SAS, Avaca LA (1998) Electrochim Acta 44:1515 doi:10.1016/S0013-4686(98)00275-8